Applied Magnetic Resonance (2019) 50:243–261
https://doi.org/10.1007/s00723-018-1062-6

Applied
Magnetic Resonance

ORIGINAL PAPER

Accelerating Parallel Magnetic Resonance Imaging Using *p*-Thresholding Based Compressed-Sensing

Irfan Ullah[1] · Omair Inam[1] · Ibtisam Aslam[1] · Hammad Omer[1]

Received: 8 June 2018 / Revised: 31 July 2018 / Published online: 4 October 2018

Abstract

Conjugate gradient-based SENSE (CG-SENSE) and compressed-sensing (CS) are well-established techniques to accelerate magnetic resonance imaging (MRI) data acquisition. CG-SENSE is an iterative parallel MRI (pMRI) technique, used for the reconstruction of unaliased MR images from the under-sampled arbitrary *k*-space trajectories (Cartesian and non-Cartesian). Whereas CS is a promising technique that requires fewer random samples in the *k*-space to speed up the data acquisition process for MR image reconstruction. In the recent past, further acceleration in MR data acquisitions has been achieved using pMRI and CS jointly. In this paper, a novel method is proposed which sequentially combines CG-SENSE with *p*-thresholding based CS to achieve higher acceleration factors without compromising the quality of image reconstruction. In the proposed method, CG-SENSE and *p*-thresholding based CS reconstructions are sequentially combined to recover aliased free images from highly under-sampled *k*-space data. The performance of the proposed method is evaluated for arbitrary *k*-space Cartesian and radial trajectories. The reconstruction results are compared with conventional methods, e.g., CG-SENSE and ℓ_1-SPIR-iT. Several experiments are performed using simulated phantom and in vivo datasets. The reconstruction quality of the proposed method is evaluated in terms of artifact power (AP), peak signal-to-noise ratio (PSNR) and root mean square error (RMSE). The experimental results show that the proposed method outperforms the CG-SENSE and ℓ_1-SPIR-iT by achieving superior image reconstruction quality.

Electronic supplementary material The online version of this article (https://doi.org/10.1007/s00723-018-1062-6) contains supplementary material, which is available to authorized users.

✉ Omair Inam
omair_inam@comsats.edu.pk

[1] Department of Electrical Engineering, COMSATS University Islamabad, Islamabad, Pakistan

1 Introduction

Magnetic resonance imaging (MRI) is a non-invasive medical imaging modality that provides essential clinical information about the anatomy and function of the human body [1]. MRI is a very powerful and versatile diagnostic imaging technique that helps the medical practitioners to treat different medical conditions. MRI is used for many clinical applications, e.g., cardiac imaging, contrast-enhanced angiography, diffusion and perfusion imaging, etc. [2]. MRI has revolutionized the medical diagnostics by providing excellent soft tissue contrast within the human body over the last decade. However, slow data acquisition is a major limitation of MRI that causes patient discomfort due to long breath hold requirements and may result in poor image quality if the patient is moving. In recent years, substantial technological improvements in the MRI hardware have helped to reduce the scan time without compromising the quality of the reconstructed images, e.g., development of fast pulse sequences [3] however, this is limited by the technical and physiological constraints [4].

Parallel magnetic resonance imaging (pMRI) techniques have been introduced in the recent past which offers an alternative way to speed-up data acquisition in MRI without degrading the quality of image reconstruction [5]. In pMRI, the reduction in scan time is achieved by collecting the under-sampled *k*-space data using multi-channel receiver coils each with a distinct sensitivity profile. The *k*-space data can be sampled along Cartesian and non-Cartesian trajectories (i.e., Radial, Spiral, PROPELLER, etc.) [6]. In pMRI, under-sampling the *k*-space data introduces aliasing artifacts in the resultant image, therefore, specialized reconstruction algorithms are used to unfold the aliased images to get the full field-of-view images, e.g., SENSE [7], SPIRiT [8], GRAPPA [9], and CGLS-RP-GRAPPA [10] are different pMRI algorithms.

Data acquisition by sampling the *k*-space along non-Cartesian trajectories (e.g., spiral [11], radial [12], PROPELLER [13], etc.) is an emerging field of research in MRI. Non-Cartesian trajectories significantly improve the speed of MRI data acquisition by increasing the efficiency of the gradient waveforms and reducing the amount of gradient encoding [14]. Compared with Cartesian sampling, non-Cartesian sampling schemes offer distinct advantages, e.g., offer more benign aliasing artifacts and provide efficient coverage of *k*-space [14].

Many pMRI methods have been proposed to reconstruct images from the under-sampled non-Cartesian *k*-space data, e.g., radial GRAPPA [15], CG-SENSE [16, 17], ESPIRiT [18], pseudo-Cartesian GRAPPA [19], etc. CG-SENSE [16, 17] algorithm is an iterative pMRI method that has the ability to recover the fully sampled MR image from the acquired under-sampled Cartesian or non-Cartesian *k*-space data. However, higher acceleration factors are difficult to achieve with CG-SENSE because of the practical limitations such as receiver coil array geometry and receiver coils sensitivity correlation [14]. In CG-SENSE if the acceleration factor exceeds certain limit, the blurring artifacts and noise amplification become more apparent in the reconstructed images [14].

Compressed-sensing (CS) is an alternative method to accelerate MRI that requires few samples in the *k*-space that are required in conventional MRI and reconstructs the unaliased image by exploiting the compressibility and sparsity of the acquired MRI data [20–22]. Since pMRI and CS techniques are used to accelerate the MR data acquisition, therefore, both can be combined to achieve further acceleration [23–25]. Combined applications using both CS and pMRI have been recently proposed for the MR image reconstruction from highly under-sampled *k*-space data points, e.g., SpRING [23], SENSECS [24], sparse SENSE [25], and ℓ_1-SPIR-iT [26, 27]. These methods show robust reconstructions with improved acceleration in data acquisition [27, 28]. SpRING, SENSECS and Sparse SENSE are limited to the MR image reconstruction using Cartesian sampling. However, ℓ_1-SPIR-iT synergistically combines the auto-calibrating pMRI with soft thresholding based CS, and accelerates the MR image reconstruction from under-sampled non-Cartesian *k*-space data (radial data) [26, 27].

This work presents a new method which sequentially combines the CG-SENSE with *p*-thresholding based CS to reconstruct MR images from the highly under-sampled Cartesian and non-Cartesian *k*-space (radial) data. The proposed method is based on the fact that noise amplification and blurring artifacts in the reconstructed image as a result of CG-SENSE reconstruction at higher acceleration factors, can be removed successfully by utilizing *p*-thresholding based CS. Therefore, in the proposed method the reconstruction outcome of CG-SENSE is fed to CS which solves the ℓ_1-minimization problem using *p*-thresholding based iterative algorithm [28–30] to recover aliased free images even at high acceleration factors.

2 Review of CG-SENSE

CG-SENSE [16] is a pMRI technique used to reconstruct MR images from the under-sampled *k*-space data (arbitrary trajectories) using multichannel receiver coil sensitivity information. Solving the unfolding problem to reconstruct unaliased image from the under-sampled non-Cartesian data in multichannel receiver coils, is a computationally expensive problem. The basic idea of CG-SENSE is to provide an alternative path to avoid the inversion (computationally intensive process) of a large generalized encoding matrix using conjugate gradient algorithm [16]. To reduce the computation expensive matrix vector multiplication during a single iteration of CG algorithm, a combination of fast Fourier-transform (FFT) with forward and reverse gridding operations are applied as shown in Fig. 1. Mathematical basis of CG-SENSE reconstruction can be described by the following equation [16]:

$$(IE^H DEI)(I^{-1}v) = IE^H Dm, \tag{1}$$

where E denotes the encoding matrix which contains all the spatial encoding information from the receiver coil sensitivities and gradients, I is a diagonal matrix which accounts for the intensity compensation of the coil weights that occurs due to the variation in coil sensitivities. D is also a diagonal matrix which accounts for density compensation (differences in the density of the sampling trajectories). v is a vector

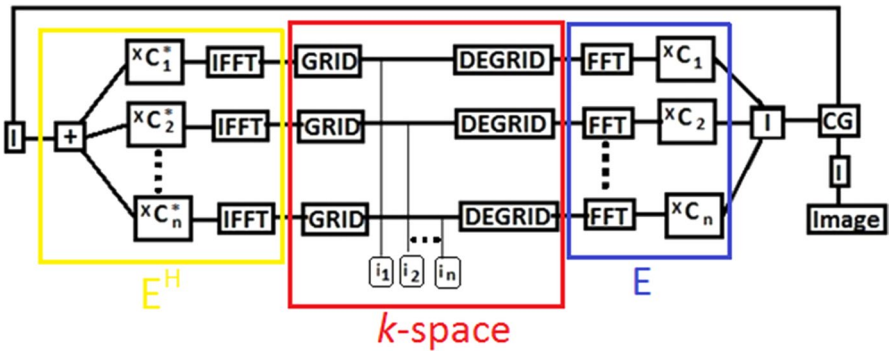

Fig. 1 CG-SENSE reconstruction [19]

of the image to be reconstructed and m shows the acquired k-space data. CG-SENSE performs image reconstruction using the following steps:

1. The right side of Eq. (1) is calculated to estimate the intermediate image a:

$$a = IE^H Dm. \tag{2}$$

2. CG determines the refined approximate solution b_{approx} to the exact solution during each iteration:

$$(IE^H DEI)b_{\text{approx}} = a. \tag{3}$$

3. When the system converges to the exact solution, the intensity-corrected reconstruction v_{approx} is performed as:

$$v_{\text{approx}} = Ib_{\text{approx}} \tag{4}$$

Figure 1 systematically demonstrates the implementation of the above given steps in CG-SENSE reconstruction process. CG-SENSE is a commonly used pMRI technique which can be easily applied to reconstruct MR images from different sampling trajectories. The output of the CG-SENSE is a reconstructed combined (sum of images from all the receiver coils) 2-D image. However, irregularity in the encoding matrix may arise due to imprecise estimation of coil sensitivities maps, resulting in residual aliasing artifacts in the reconstructed images especially at higher acceleration factors.

3 Review of Compressed-Sensing (CS)

CS is an efficient way for performing MR image reconstruction without the loss of information from fewer data samples (also called incoherent measurements) [20]. For CS based MR reconstructions following conditions need to be satisfied [20]:

- The desired image should have sparse representation in a known transform domain.
- Under-sampling the *k*-space should cause incoherent (noise like) artifacts in a sparsifying transform domain.
- Non-linear reconstruction method should be used, which enforces both the sparsity of the image representation and consistency of reconstruction with the acquired samples.

Some MR images are naturally sparse while others can be made sparse by applying some sparsifying transform. A sparsifying transform is an operator which maps a vector of image data to a sparse vector, e.g., wavelet transform (WT) and discrete cosine transform (DCT). Recovery of a transform sparse signal from incomplete measurements is represented as [20]:

$$\min_{g} \|g\|_1, \tag{5}$$

$$\text{s.t.} \quad y = F_{\text{u}} g,$$

where g denotes the reconstructed image. y is the under-sampled k-space data (measured data), F_{u} represents the Fourier transform. If $g = \psi x$, where ψ represents a sparsifying transform, then the measured data can be expressed as [20]:

$$\min_{x} \|x\|_1 \tag{6}$$

$$\text{s.t.} \quad y = F_{\text{u}} \psi^{\text{T}} x = Mx,$$

where $M = F_{\text{u}} \psi^{\text{T}}$ represents the under-sampling mask with Fourier encoding. Since y is the under-sampled k-space data which may often contain noise, therefore, Eq. (6) can be solved using the following constraint:

$$\min_{x} \|x\|_1, \tag{7}$$

$$\text{s.t.} \quad y = \|y - Mx\|_2 < \epsilon.$$

The constraint $\|y - Mx\|_2 < \epsilon$ enforces the data consistency with the acquired data such that Eq. (6) finds a solution which is compressible by the transform ψ. The parameter ϵ is usually set below the expected noise level. The MR reconstruction problem using Eq. (7) becomes ill-posed, because there are few measured signals y than the unknowns x. Therefore, the problem in Eq. (7) becomes highly underdetermined and has infinite many solutions. Regularization techniques can be used to restore stability in the reconstruction problem (Eq. 7) where prior information about the image can also be incorporated effectively [22, 30]. With the advent of CS theory, sparsity-promoting regularization criteria have gained popularity in MRI [31].

The MR reconstruction problem for CS consists of both sparsity and data consistency, which can be expressed by the Lagrangian constraint as [20]:

$$\min_{g} \|y - Mx\|_2^2 + \tau \|g\|_1. \tag{8}$$

In Eq. (8), the first term is the data fidelity term, whereas the second term τ represents the regularization parameter defining the contribution of the prior information. The MRI-CS reconstruction quality depends on the under-sampled Fourier transform (F_u) and sparsifying transform (ψ). Wavelet transform and total variation (TV) based constraints can be used to improve the image reconstruction quality [32, 33]. Wavelet transform is used to sparsify the image by transforming the image into wavelet coefficients at different scales, whereas TV-based constraint preserves the edges in the MR image [20]. The final image is reconstructed from the under-sampled k-space data by solving Eq. (8) as a constrained convex optimization problem [20]

$$\min_{g} \left\{ \frac{1}{2} \|F_u g - y\|_2^2 + \alpha \|g\|_{TV} + \beta \|\psi g\|_1 \right\}, \tag{9}$$

where α and β are line search parameters and TV can be expressed as [20].

$$g_{TV} = \sum_a \sum_b \sqrt{\left(\nabla_x g_{ab}\right)^2 + \left(\nabla_y g_{ab}\right)^2}, \tag{10}$$

where ∇_x and ∇_y denote the finite differences along x and y coordinates.

It has been shown in both theoretical and experimental studies [34–36] that the solution to the sparse representation with ℓ_p-norm minimization problem ($0 \le p < 1$) shown in the following equation, is closer to the sparse representation of ℓ_1-norm minimization problem given in Eq. (8).

$$\min_{g} \left\| y - Mx_2^2 \right\| + \tau \left\| g_p^p \right\|. \tag{11}$$

In CS-MRI, the image restoration can be better modeled using $0 \le p < 1$ in Eq. (11) [30]. Many algorithms have been used for solving ℓ_p-norm minimization problem given in Eq. (11), e.g., iteratively reweighted least square (IRLS) [37], iteratively reweighted ℓ_1-minimization (IRL1) [38], iteratively thresholding method (ITM-ℓ_p) [39], and look-up-table (LUT) [40]. However, the performance of the IRLS, IRL1 and ITM-ℓ_p suffers due to an inaccurate convergence to the optimal solution [41]. However, LUT involves more computation and storage cost if p changes dynamically [40]. Recently, p-thresholding based generalized iterative shrinkage algorithm [28, 41] has been used for solving ℓ_p-norm minimization problem (Eq. 11) using arbitrary values of p and τ. It has been demonstrated [41] that the p-thresholding based generalized iterative shrinkage algorithm converges to more accurate solution as compared to IRLS, IRL1 and ITM-ℓ_p.

4 Proposed Method: CG-SENSE Combined with *p*-Thresholding Based Compressed-Sensing

In this work, a new method is presented which sequentially combines the CG-SENSE with *p*-thresholding based compressed-sensing for accelerated MRI data acquisitions (Cartesian and non-Cartesian). The proposed method is based on the fact that noise amplification and blurring artifacts (which are more prominent at higher acceleration factors) in the reconstructed image as a result of CG-SENSE reconstruction, can be removed successfully by applying *p*-thresholding based CS. The flow diagram of the proposed method is shown in Fig. 2.

The first step in the proposed method is to receive the under-sampled (non-Cartesian/Cartesian) *k*-space data from the multichannel receiver coils. In the second step, density compensation is applied on the acquired *k*-space data and gridding is performed to map the non-Cartesian data in each channel to the Cartesian gird. The gridding process is followed by the application of fast Fourier-transform (FFT) and the resulting images from the multichannel receiver coils are multiplied with the complex conjugate of the receiver coil sensitivities and summed to produce a single image. Subsequent intensity corrected image defined by a vector a as given in Eq. (2), is used for initializing the CG algorithm (see pseudo code of proposed algorithm given in appendix A as a supplementary material) and the first iteration starts with $b_{\text{approx}(0)} = 0, \quad s_0 = a$. Each iteration of CG algorithm performs multiplication of $\left(IE^{\mathrm{T}}DEI\right)$ with the residual vector $\left(s_i\right)$ from the previous iteration and determines a refined approximate image $(b_{\text{approx}(i)})$ using Eq. (3). After executing the CG algorithm for the minimum number of iterations $(I_{\min})$ that are required to obtain the reconstruction result with lowest possible errors, the resultant image is processed by *p*-thresholding based CS to attain acceptable predefined tolerance level $\left(\emptyset = 10^{-4}\right)$. In *p*-thresholding based CS, iterative soft thresholding algorithm (ISTA) based on *p*-thresholding technique [29, 30] has been introduced to solve the problem given in Eq. (8), using the following equation:

$$x_{j+1} = C_{(\tau,p)_j}\left(x_j + M^{\mathrm{T}}\left(y - Mx_j\right)\right), \tag{12}$$

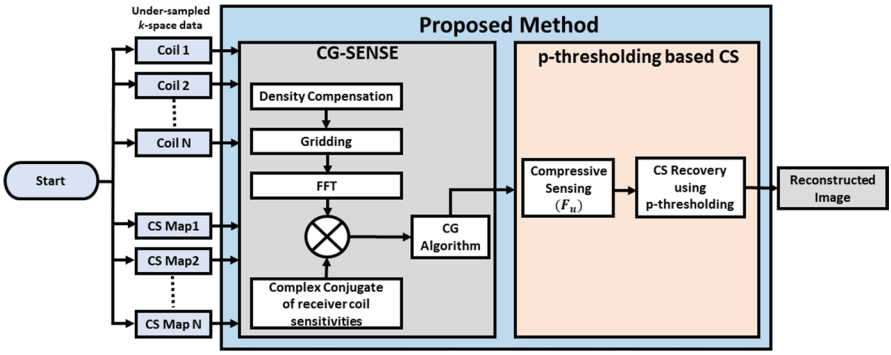

Fig. 2 Block diagram of the proposed method

where x_j represents a vectorized representation (coefficient vector) of the image to be reconstructed in jth iteration and y denotes the measured data. The operator $M = F_u \psi^T$ represents the encoding matrix to find the sparsest possible solution in ψ transform domain. $C_{(\gamma,p)}$ denotes the thresholding function with thresholding parameter τ. p is the value which adds weights to the elements of the coefficient vector x. The smaller value of p is associated with strong sparsity [30]. The value of τ follows a decaying update with each iteration by a factor α (Appendix A in supplementary material). The value of α can be initialized in the range between 0 and 1 [30]. However, the algorithm converges rapidly for small values of α [30]. The thresholding function $C_{(\tau,p)}$ is defined as [28]:

$$(C_{(\tau,p)})_j = \text{sgn}(x_j)\max\left\{0, \left|x_j\right| - \tau_k \left|x_j\right|^{p-1}\right\}. \tag{13}$$

The pseudo code of ISTA based p-thresholding technique is given in Appendix A of supplementary material. The algorithm starts the first iteration with $x_0 = 0$ and y is the output image from CG-SENSE (containing blurring artifacts and noise at higher acceleration factors). During each iteration, the algorithm performs thresholding on the sparse coefficients $\left(x_j\right)$ of the reconstructed image and minimizes the residual $\left(y - Mx_j\right)$ using gradient descent algorithm. Each iteration results in a refined approximation $\left(x_j\right)$ to minimize the residual error ($e_{j+1} = y - Mx_j$). The iterations stop when the following condition is met [30]:

$$\epsilon < \frac{y - Mx_{j2}}{y_2}. \tag{14}$$

As soon as the iterations are stopped, the coefficients $\left(x_j\right)$ of the last iteration are multiplied by ψ^T to yield the final reconstructed image.

5 Materials and Methods

5.1 Datasets

The proposed algorithm is evaluated using both the simulated and in vivo datasets. To evaluate the non-Cartesian image reconstruction using the proposed method, the sensitivity profiles of 12 channel circular coils were analytically modeled using Biot–Savart equations [42]. The simulated sensitivity profiles are applied on Shepp–Logan phantom to obtain simulated Shepp–Logan phantom images with coil sensitivity information. The resultant simulated image ($256 \times 256 \times 12$) is Fourier-transformed to produce Cartesian k-space data and then sinc interpolations [43] are used to resample the Cartesian k-space data points into 400 radial projections having 256 readout points per projection.

For in vivo study, the proposed method is tested on two fully sampled MRI datasets. (1) Human head data ($256 \times 256 \times 8$) acquired using 1.5 T GE scanner (St. Mary's Hospital London) with 8 channel head coils, FOV = 200 mm^2,

TR/TE = 500/10 ms, slice thickness = 3 mm, and flip angle = 50°. (2) Human head data acquired (448 × 224 × 12) using 3.0 T Siemens Skyra scanner at Case Western Reserve University, Cleveland, OH, USA with 12-channel head coils, FOV = 230 mm^2, TR/TE = 938/7.2 ms, slice thickness = 5 mm and flip angle = 58°.

Informed written consent of the volunteers was obtained before each study, in compliance with the guidelines of Institutional Review Board for Human Studies at University Hospitals of Cleveland, Case Western Reserve University (CWRU), and St. Mary's Research Ethics Committee (REC).

5.2 Simulation and Evaluations Parameters

To validate the performance of the proposed method with under-sampled non-Cartesian MRI data acquisitions, the radial *k*-space data of simulated Shepp–Logan phantom was retrospectively under-sampled at various acceleration factors, i.e., $(4 \leq R \leq 12)$, whereas the acquired fully sampled 8-channel human head Cartesian dataset (256 × 256 × 8) is initially resampled into fully sampled radial dataset with 402 radial projections (using Fessler toolbox available at http://web.eecs.umich.edu/~fessler/code/index.html). The total number of projections required for the fully sampled radial dataset are determined as [14]: $\left(\frac{\pi}{2}\right) \times 256 = 402$. The fully sampled 8-channel human head radial data is then retrospectively under-sampled by taking a portion of the fully sampled radial spokes, at acceleration factors $R = 6$, 8 and 12. In this paper, the acceleration factors (R) for the radial data are determined with respect to the Nyquist limit as $\left(R = \frac{\text{No. of projections in the fully sampled data}}{\text{No. of projections in the undersampled data}}\right)$ [14]. To validate the performance of the proposed method with accelerated Cartesian acquisitions, the 12-channel human head dataset is retrospectively under-sampled at acceleration factors $R = 6$ and 8.

The parameters used in Eqs. (12) and (13) for the iterative *p*-thresholding are $\tau = \max\left(M^{\mathrm{T}} e_0\right)$ [30] (also see Appendix A in supplementary material), $\alpha = 0.1$, $p = -2.5$ [30] and $\epsilon = 10^{-6}$. The value of α is optimally selected to minimize the reconstruction errors with respect to the fully sampled data. The Matlab code of iterative *p*-thresholding is available at http://miprg.com/downloads/.

For the comparison purpose, reference images (gold standard) were obtained from the fully sampled datasets of all the receiver coils using sum-of-squares reconstruction. The reconstruction quality of the proposed method was compared with CG-SENSE and ℓ_1-SPIR-iT by measuring the artifact power (AP) [44], peak signal-to-noise ratio (PSNR) [45] and root mean Square Error (RMSE) [45] in the reconstructed images. Moreover, the reconstructed images using the proposed method, CG-SENSE and ℓ_1-SPIR-iT are shown individually on the same scale for visual evaluation of the image noise, artifacts, and resolution. In this paper the reconstructions are performed in MATLAB (Mathworks, Natick, MA) and run on Hewlett-Packard ZBook (i7-4800MQ) workstation with a 2.7-GHz CPU, 2-GB NIVIDIA Quadro 2100 GPU and 8-GB RAM. ℓ_1-SPIR-iT is implemented using Berkeley

Advanced Reconstruction Toolbox (BART) [46] free and open-source image-reconstruction framework for MRI (available at https://mrirecon.github.io/bart/).

6 Results and Discussion

This paper presents a new method which sequentially combines CG-SENSE with p -thresholding based Compressed-Sensing to produce high quality images from the under-sampled data (Cartesian and non-Cartesian). To compare the performance of the proposed method with CG-SENSE and ℓ_1-SPIR-iT, the reconstructions are performed on the simulated radial datasets of Shepp–Logan phantom ($256 \times 256 \times 12$) with different acceleration factors ($4 \leq R \leq 12$). The reconstruction quality in terms of root mean square error (RMSE) and artifact power (AP) for each method is plotted (Figs. 3, 4, 5) against different acceleration factors (R) ranging from 4 to 12. The results show that the CG-SENSE and ℓ_1-SPIR-iT show a rapid increase in the RMSE and AP values of the reconstructed images at higher acceleration factors, hence degrading the quality of image reconstruction. However, the proposed method achieves higher acceleration factors without significant degradation in the quality of the reconstructed image as compared to CG-SENSE and ℓ_1-SPIR-iT. It can be observed in Figs. 3 and 4, that the proposed method is able to reconstruct images with lower RMSE and AP values at different acceleration factors, as compared to CG-SENSE and ℓ_1-SPIR-iT, e.g., for acceleration factor (R) 4, the proposed method improves the quality of image reconstruction by demonstrating ~71% less

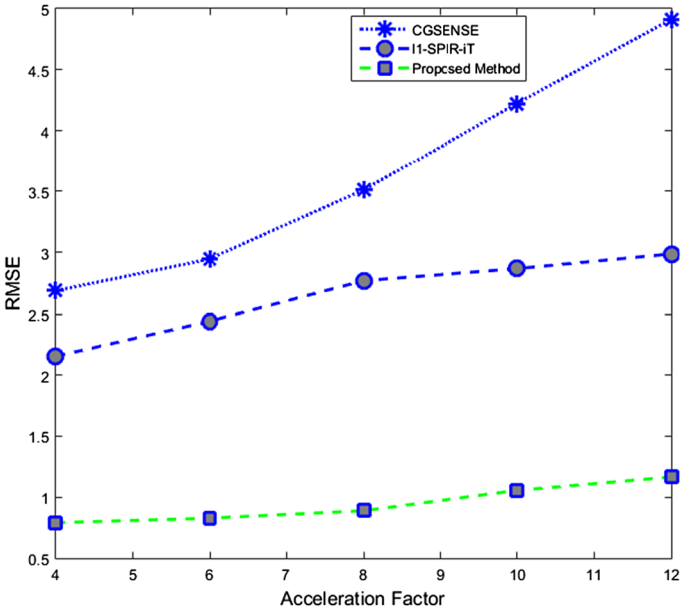

Fig. 3 Comparison of the RMSE values between the proposed method, CG-SENSE and ℓ_1-SPIR-iT at various acceleration factors for Shepp–Logan phantom dataset

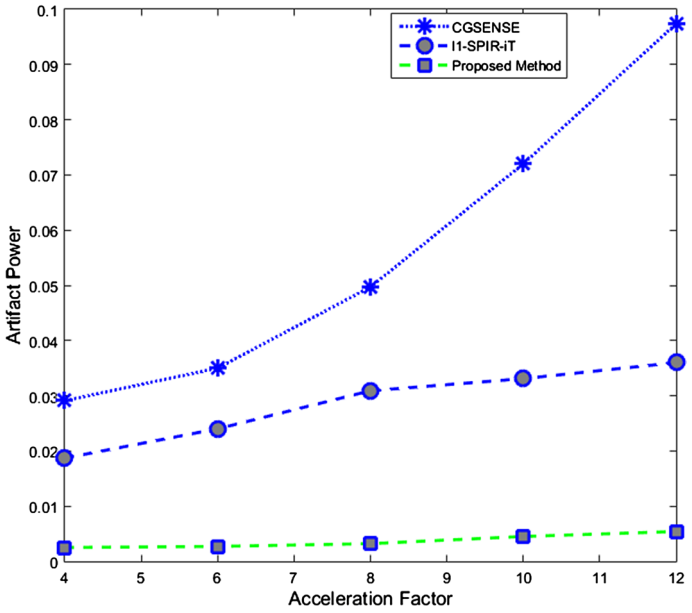

Fig. 4 Comparison of artifact power (AP) achieved by the proposed method, CG-SENSE and ℓ_1-SPIR-iT for Shepp–Logan phantom dataset

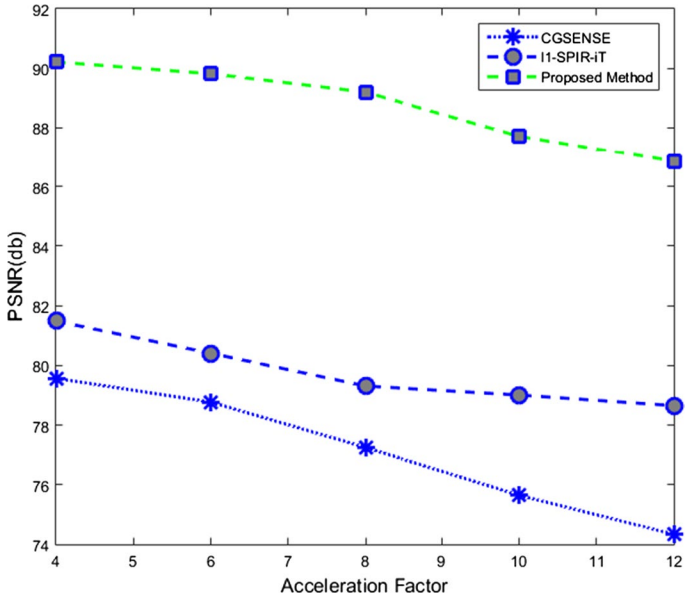

Fig. 5 Comparison of the reconstruction quality in terms of PSNR between the proposed method, CG-SENSE and ℓ_1-SPIR-iT for Shepp–Logan phantom dataset

RMSE and ~91% less AP in the reconstructed images as compared to CG-SENSE (see Figs. 3, 4). This trend continues even at higher acceleration factors, e.g., for $R=12$, the proposed method exhibits ~76% less RMSE and ~94% less AP in the reconstructed images as compared to CG-SENSE. Similarly, for $R=4$, the proposed method shows ~63% reduction in RMSE and ~87% reduction in AP of the reconstructed image as compared to ℓ_1-SPIR-iT, whereas for $R=12$, the proposed method achieves ~61% reduction in RMSE and ~85% reduction in AP of the reconstructed image as compared to ℓ_1-SPIR-iT.

For further evaluation, PSNR values of the reconstructed images using the proposed method, CG-SENSE and ℓ_1-SPIR-iT are plotted (Fig. 5) against different acceleration factors ($4 \leq R \leq 12$). The results show that PSNR of the reconstructed images by CG-SENSE and ℓ_1-SPIR-iT, is largely affected by the noise induced due to the under-sampling of the k-space at higher acceleration factors ($R>8$). However, the proposed method is able to reconstruct the images with higher PSNR against different acceleration factors ($4 \leq R \leq 12$).

For visual comparison of the reconstruction accuracy of the proposed method with CG-SENSE and ℓ_1-SPIR-iT, the reconstructed images of 12-channel radial datasets of the simulated Shepp–Logan phantom for different number of radial projections corresponding to acceleration factors, i.e., $R=6$, $R=8$ and $R=12$, are shown in Fig. 6. The reference image was obtained from the fully sampled dataset ($256\times256\times12$) and is shown at the top left corner of Fig. 6. A magnified section of each image is shown for better visualization of the reconstruction quality. In Fig. 6, the first column shows the reconstruction results of CG-SENSE, ℓ_1-SPIR-iT and the proposed method for acceleration factor (R) 6, whereas 2nd and 3rd columns show the reconstruction results with $R=8$ and $R=12$, respectively. The results (Fig. 6) show that severity of the blurring and moire artifacts in the reconstructed images using CG-SENSE and ℓ_1-SPIR-iT, is related to the extent of the k-space that has been reduced to simulate the accelerated radial data acquisitions (i.e., $R=6$, $R=8$ and $R=12$). For example, the results shown in Fig. 6 validate that the reconstructed images using CG-SENSE and ℓ_1-SPIR-iT contain the noisy edges and visible blurring and moire artifacts for acceleration factors (R) 8 and 12, resulting in low peak-signal-to-noise ratio (PSNR) (Fig. 5), large root-mean-square error (RMSE) (Fig. 3) and high artifact power (AP) (Fig. 4). However, the proposed method successfully reduces the noise and decreases the blurring and moire artifacts in the reconstructed images thereby achieving better reconstruction quality visually and quantitatively as compared to CG-SENSE and ℓ_1-SPIR-iT. For example, for $R=12$, the proposed methods significantly suppress the noise enhancements and reduce the blurring and moire artifacts in the reconstructed images as compared to CG-SENSE (Fig. 6), whereas for $R=12$, the proposed method improved the reconstruction results of CG-SENSE by increasing PSNR of the reconstructed image from 74.33 to 86.85 dB (Fig. 5) and reducing RMSE and AP values from 4.913 to 1.162 (Fig. 3) and from 0.097 to 0.0054 (Fig. 4) respectively. Similarly for $R=12$, the proposed method demonstrate substantial improvements in the quality of image reconstruction by reducing the blurring and moire artifacts in the reconstructed images as compared to the ℓ_1-SPIR-iT (Fig. 6), whereas for $R=12$, the proposed method improved the reconstruction quality of ℓ_1-SPIR-iT by increasing PSNR of the reconstructed image

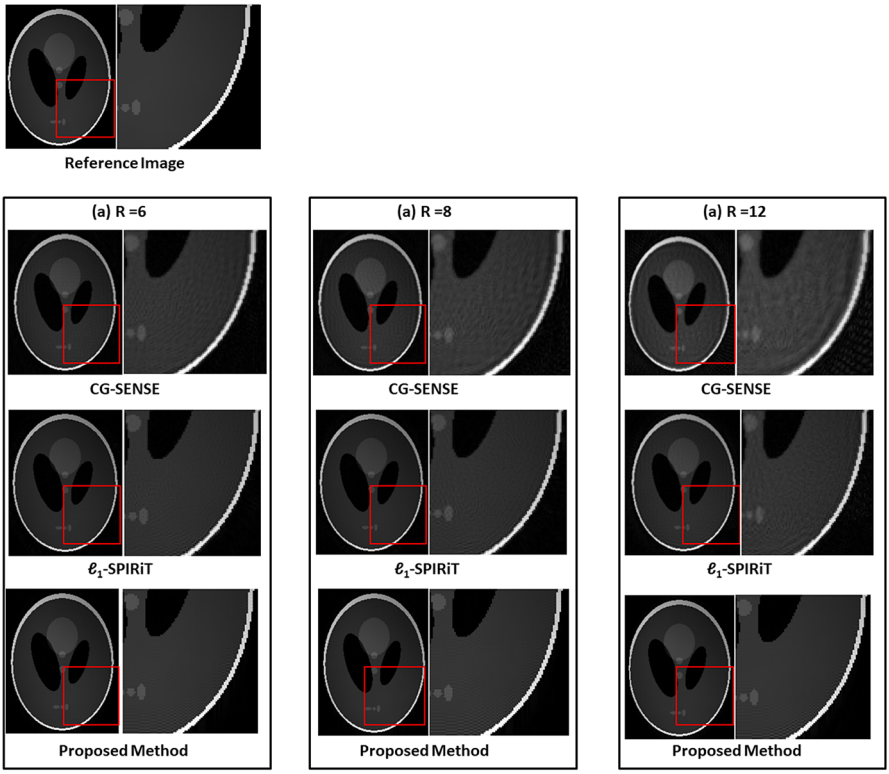

Fig. 6 Reconstructed images of 12-channel radial dataset of the simulated Shepp–Logan phantom with radial projections corresponding to acceleration factors $R=6$, $R=8$ and $R=12$, using CG-SENSE, ℓ_1 -SPIR-iT and the proposed method

from 78.65 to 86.85 dB (Fig. 5) and reducing RMSE and AP values from 2.99 to 1.162 (Fig. 3) and from 0.036 to 0.0054 (Fig. 4) respectively.

Several experiments using in vivo dataset are also performed to validate the performance of the proposed methods in terms of reconstruction accuracy for different acceleration factors. For this, the fully sampled radial dataset of human head ($256\times256\times8$) is retrospectively under-sampled at acceleration factors $R=8$ and 12. The reconstruction results for in vivo 1.5 T human head in terms of RMSE, AP and PSNR are given in Table 1 and Table 2 to compare the reconstruction quality of the proposed method with CG-SENSE and ℓ_1-SPIR-iT. The results show (see Table 1) that for acceleration factor 8, the proposed method achieves better reconstruction accuracy as compared to CG-SENSE and ℓ_1-SPIR-iT, by reconstructing images with higher PSNR, lower RMSE and lower AP values, e.g., for $R=8$ the reconstructed images using the proposed method (Table 1) contain ~75% less RMSE and ~94% less AP and 15% more PSNR, as compared to the reconstructed images using CG-SENSE, whereas the proposed method achieves 59% less RMSE, 83% less AP and 9% more PSNR in the reconstructed images as compared to ℓ_1-SPIR-iT. Table 2

Table 1 Comparison of the reconstruction quality (in terms of RMSE, AP and PSNR) for 1.5 T human head image at acceleration factor 8 between CG-SENSE, ℓ_1-SPIR-iT and proposed method

Acceleration factor	Reconstruction methods	RMSE	AP	PSNR (dB)
8	CG-SENSE	3.0504	0.0151	78.4778
	ℓ_1-SPIR-iT	1.8313	0.0054	82.91
	Proposed Method	0.7597	0.000938	90.5519

Table 2 Comparison of the reconstruction quality (in terms of RMSE, AP and PSNR) for 1.5 T human head image at acceleration factor 12 between CG-SENSE, ℓ_1-SPIR-iT and proposed method

Acceleration factor	Reconstruction methods	RMSE	AP	PSNR (dB)
12	CG-SENSE	5.0931	0.0421	74.0251
	ℓ_1-SPIR-iT	2.7021	0.0119	79.531
	Proposed method	0.9651	0.001500	88.4738

gives the reconstruction results (in terms of RMSE, AP and PSNR) of the proposed method, CG-SENSE and ℓ_1-SPIR-iT for $R=12$. The results show that the proposed method provides up to 81% improvement in terms of RMSE, 96% improvement in terms of AP and 20% improvements in terms of PSNR as compared to CG-SENSE. Whereas 64% improvement in terms of RMSE, 87% improvement in terms of AP and 11% improvements in terms of PSNR is reported for the proposed method on 1.5 T human head dataset, as compared to the ℓ_1-SPIR-iT.

Figure 7 shows the reconstruction results of the human head data (acquired using 1.5 T GE scanner) using CG-SENSE, ℓ_1-SPIR-iT and the proposed method at acceleration factors $R=8$ and $R=12$. The reference image was obtained from the fully sampled dataset ($256\times256\times8$) and is shown at the top left corner of Fig. 7. To better visualize and compare the reconstruction quality of the proposed method with CG-SENSE and ℓ_1-SPIR-iT, a magnified section of the reconstructed image is shown for each reconstruction method. The results show that the proposed method successfully removes the blurring artifacts and noisy edges in the reconstructed images for $R=8$ and $R=12$, thereby achieving better reconstruction quality for accelerated data acquisitions as compared to CG-SENSE and ℓ_1-SPIR-iT.

To further validate the performance of the proposed method to reconstruct aliased free MR images from the under-sampled Cartesian data, we performed several experiments using 12-channel in vivo human head data ($448\times224\times12$) obtained using 3 T Siemens Skyra scanner. To simulate the accelerated data acquisitions, the fully sampled *k*-space data of each receiver coil is retrospectively under-sampled in the phase encoding direction by acceleration factors $R=6$ and $R=8$. To compare the performance of the proposed method with CG-SENSE and ℓ_1-SPIR-iT, the reconstruction results of each method are given in Tables 3 and 4. The results (Table 3) show that for $R=6$, the proposed method achieves higher PSNR, lower RMSE and lower AP values as compared to CG-SENSE(i.e., ~77% less RMSE, ~96% less

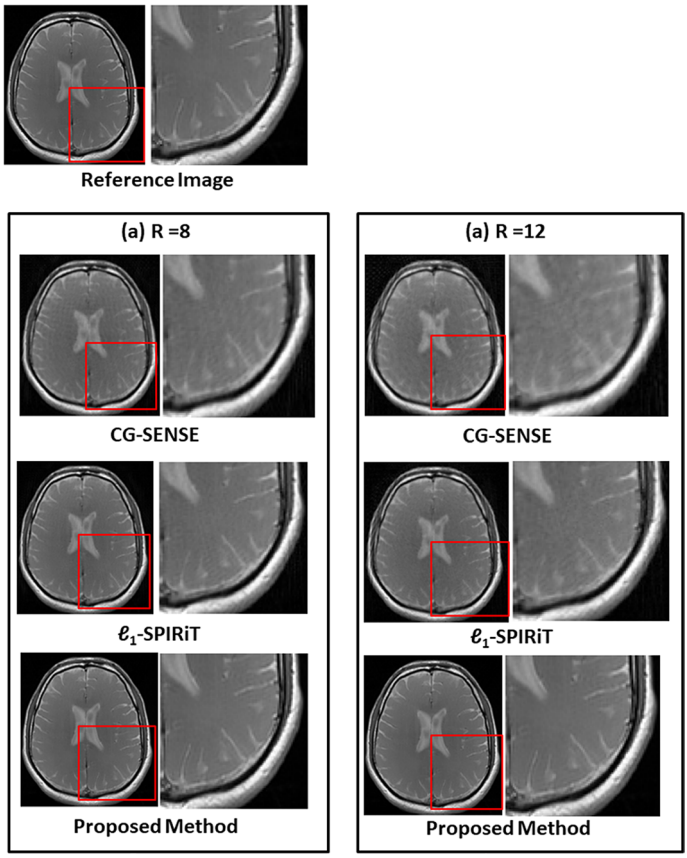

Fig. 7 1.5 T axial brain images of 8-channel human head data with radial projections corresponding to acceleration factors $R=8$ and $R=12$, using CG-SENSE, ℓ_1-SPIR-iT and the proposed method

Table 3 Comparison of the reconstruction quality of 12-channel 3 T human head image retrospectively under-sampled at acceleration factor 6 between CG-SENSE, ℓ_1-SPIR-iT and proposed method in terms of RMSE, AP and PSNR

Acceleration factor	Reconstruction methods	RMSE	AP	PSNR (dB)
6	CG-SENSE	4.23	0.031	72.123
	ℓ_1-SPIR-iT	2.43	0.0091	75.123
	Proposed method	0.982	0.0012	85.234

AP and 18% higher PSNR) and ℓ_1-SPIR-iT(achieves 60% less RMSE, 87% less AP and 13% higher PSNR). Table 4 shows the reconstruction results of the proposed method, CG-SENSE and ℓ_1-SPIR-iT using $R=8$. The results show that the proposed method provides up to 87% improvement in terms of RMSE, 93% improvement in terms of AP and 14% improvements in terms of PSNR, as compared to CG-SENSE, whereas 76% improvement in terms of RMSE, 86% improvement in terms of AP

Table 4 Comparison of the reconstruction quality of 12-channel 3 T human head image retrospectively under-sampled at acceleration factor 8 between CG-SENSE, ℓ_1-SPIR-iT and proposed method in terms of RMSE, AP and PSNR

Acceleration factor	Reconstruction methods	RMSE	AP	PSNR (dB)
8	CG-SENSE	7.89	0.061	70.432
	ℓ_1-SPIR-iT	4.212	0.03122	72.345
	Proposed method	1.01	0.004300	80.2123

and 11% improvements in terms of PSNR is reported using the proposed method as compared to the ℓ_1-SPIR-iT.

Figure 8 shows the reconstructed images for different acceleration factors (12-channel human head data obtained from 3 T Siemens Skyra scanner) using

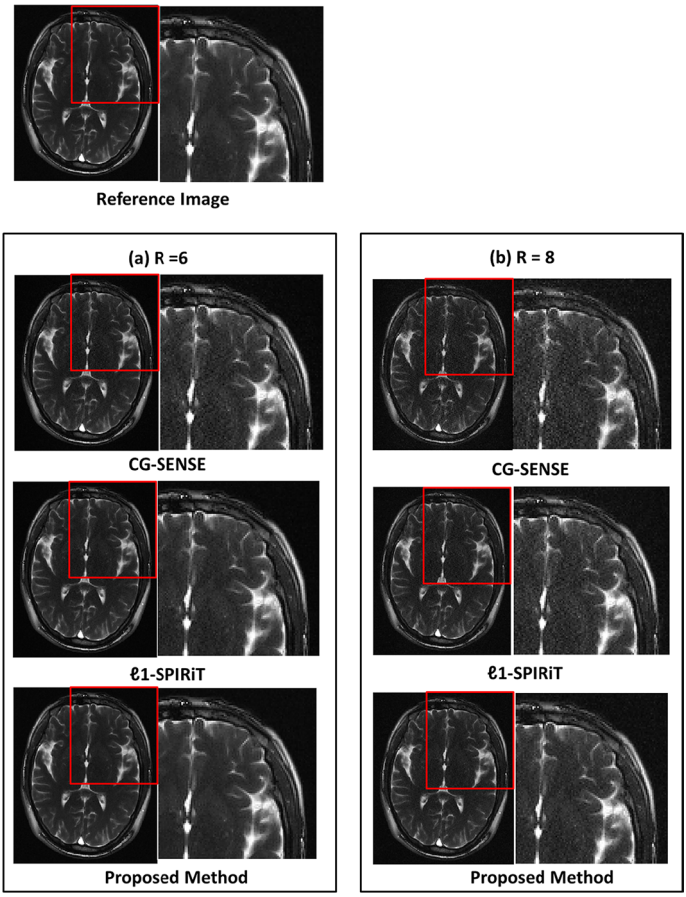

Fig. 8 3 T human brain images of 12-channel Cartesian dataset with different acceleration factors, i.e., $R=6$ and $R=8$, using CG-SENSE, ℓ_1-SPIR-iT and the proposed method

the proposed method, CG-SENSE and ℓ_1-SPIR-iT. The reference image is shown at the top left corner of Fig. 8. The results show that CG-SENSE and ℓ_1-SPIR-iT reconstructions introduce noise and blurring artifacts in the reconstructed images at AF = 6 and AF = 8. However, ℓ_1-SPIR-iT shows slightly better reconstruction results as compared to CG-SENSE. The ℓ_1-SPIR-iT is a parallel imaging method based on auto-calibration method for the estimation of sensitivity maps [25], where the sensitivity map estimations for each receiver coil rely on the information acquired from the center of the *k*-space. Therefore, any loss of information or noise at the center of the *k*-space may result in improper estimations of coil sensitivity profiles, thereby degrading the quality of image reconstruction especially at higher acceleration factors. However, in the proposed method, the sensitivity maps are acquired using prescan method [47]. Moreover, the proposed method exploits the characteristics [28, 30] of *p*-thresholding to preserve more image details with an acceptable level of noise in the reconstructed image, thereby achieving better reconstruction quality as compared to CG-SENSE and ℓ_1-SPIR-iT.

To summarize the above discussion, the proposed method clearly outperforms the CG-SENSE and ℓ_1-SPIR-iT reconstructions by preserving structure and recovering more information in the reconstructed images at different acceleration factors, thereby demonstrating better reconstruction results in terms of RMSE, AP and PSNR as compared to contemporary methods.

7 Conclusion

A new method is presented which sequentially combines the CG-SENSE with *p* -thresholding based CS to remove the noise amplification and blurring artifacts (which occurred because of under-sampling) in the reconstructed images. The performance of the proposed method is evaluated in terms of RMSE, AP and PSNR of the reconstructed images. The reconstruction results are compared with CG-SENSE and ℓ_1-SPIR-iT. Experimental results demonstrate that higher acceleration factors can be achieved with the proposed method without compromising the quality of image reconstruction, e.g., in the case of 8-channel human head radial dataset with acceleration factor 12, the proposed method achieves ~81% less RMSE, ~96% less AP and ~20% higher PSNR as compared to CG-SENSE. However, for the same dataset, the proposed method demonstrates ~64% less RMSE, ~87% less AP and ~11% higher PSNR for acceleration factor 12 as compared to the ℓ_1-SPIR-iT.

References

1. D.W. McRobbie, E.A. Moore, M.J. Graves, M.R. Prince, *MRI from Picture to Proton* (Cambridge University Press, Cambridge, 2007)
2. A.G. van der Kolk, J. Hendrikse, J.J. Zwanenburg, F. Visser, P.R. Luijten, Eur. J. Radiol. **82**, 708–718 (2013)
3. M.A. Bernstein, K.F. King, X.J. Zhou, *Handbook of MRI Pulse Sequences* (Elsevier, New York, 2004)

4. R.J. Stafford, in *Proceedings of the 46th Annual Meeting of American Association of Physicists in Medicine AAPM* (Pittsburgh, Pensnsylvania, 25–29 July 2004), p. 1836
5. S.O. Schoenberg, A. Baert, O. Dietrich, M.F. Reiser, *Parallel Imaging in Clinical MR Applications* (Springer, Berlin, 2007)
6. A. Deshmane, V. Gulani, M.A. Griswold, N. Seiberlich, J. Magn. Reson. Imaging **36**, 55–72 (2012)
7. I. Ullah, H. Nisar, H. Raza, M. Qasim, O. Inam, H. Omer, Comput. Biol. Med. **95**, 1–12 (2018)
8. M. Lustig, J.M. Pauly, Magn. Reson. Med. **64**, 457–471 (2010)
9. M.A. Griswold, P.M. Jakob, R.M. Heidemann, M. Nittka, V. Jellus, J. Wang, B. Kiefer, A. Haase, Magn. Reson. Med. **47**, 1202–1210 (2002)
10. O. Inam, M. Qureshi, S.A. Malik, H. Omer, BioMed Res. Int. **2017**, 3872783 (2017)
11. A. Tolouee, J. Alirezaie, P. Babyn, J. Magn. Reson. **260**, 10–19 (2015)
12. G. Glover, J. Pauly, Magn. Reson. Med. **28**, 275–289 (1992)
13. J.G. Pipe, Magn. Reson. Med. **42**, 963–969 (1999)
14. K.L. Wright, J.I. Hamilton, M.A. Griswold, V. Gulani, N. Seiberlich, J. Magn. Reson. Imaging **40**, 1022–1040 (2014)
15. M.A. Griswold, R.M. Heidemann, P.M. Jakob, in *Proceedings of the 11th Annual Meeting of the International Society for Magnetic Resonance in Medicine (ISMRM)* (Toronto, Ontario, Canada, 10–16 July 2003), vol. 2349
16. K.P. Pruessmann, M. Weiger, P. Börnert, P. Boesiger, Magn. Reson. Med. **46**, 638–651 (2001)
17. M. Khan, T. Aslam, H. Shahzad, H. Omer, Appl. Magn. Reson. **48**, 227–240 (2017)
18. I. Aslam, F. Najeeb, H. Omer, Appl. Magn. Reson. **49**, 107–124 (2018)
19. N. Seiberlich, F. Breuer, R. Heidemann, M. Blaimer, M. Griswold, P. Jakob, Magn. Reson. Med. **59**, 1127–1137 (2008)
20. M. Lustig, D. Donoho, J.M. Pauly, Magn. Reson. Med. **58**, 1182–1195 (2007)
21. J. Shah, I. Qureshi, J. Proano, Y. Deng, Appl. Magn. Reson. **46**, 837–851 (2015)
22. M. Kaleem, M. Qureshi, H. Omer, Appl. Magn. Reson. **47**, 415–428 (2016)
23. D.S. Weller, J.R. Polimeni, L. Grady, L.L. Wald, E. Adalsteinsson, V.K. Goyal, in *Proceedings of the 2011 IEEE International Conference on Acoustics, Speech and Signal Processing (ICASSP)* (Prague, Czech Republic, 22–27 May 2011), pp. 553–556
24. B. Wu, R.P. Millane, R. Watts, P.J. Bones, Magn. Reson. Med. **65**, 83–95 (2011)
25. D. Liang, B. Liu, J. Wang, L. Ying, Magn. Reson. Med. **62**, 1574–1584 (2009)
26. M. Lustig, M. Alley, S. Vasanawala, D.L. Donoho, J.M. Pauly, in *Proceedings of the 17th Annual ISMRM Scientific Meeting and Exhibition 2009* (Honolulu, Hawaii ,18–24 April 2009), vol. 17, p. 379
27. M. Murphy, M. Alley, J. Demmel, K. Keutzer, S. Vasanawala, M. Lustig, IEEE Trans. Med. Imaging **31**, 1250–1262 (2012)
28. S. Voronin, R. Chartrand, in *Proceedings of the 2013 IEEE International Conference on Acoustics, Speech and Signal Processing (ICASSP)* (Vancouver, British Columbia, Canada, May 26–31, 2013), pp. 1636–1640
29. I. Daubechies, M. Defrise, C. De Mol, Commun. Pure Appl. Math. **57**, 1413–1457 (2004)
30. S. Elahi, H. Omer, J. Magn. Reson. **286**, 91–98 (2018)
31. X. Zhang, M. Burger, X. Bresson, S. Osher, SIAM Imaging Sci. **3**, 253–276 (2010)
32. M.P. Romaniuk, Ph.D Thesis, Imperial College London, London, UK (2016)
33. S. Xie, W. Huang, Z. Lu, S. Huang, C. Guan, in *Proceedings of the 2017 IEEE 2nd International Conference on Signal and Image Processing (ICSIP)* (Singapore, August 4–6, 2017), pp. 193–197
34. M. Çetin, W.C. Karl, IEEE Trans. Image Process. **10**, 623–631 (2001)
35. R. Chartrand, IEEE Signal Process. Lett. **14**, 707–710 (2007)
36. R. Chartrand, V. Staneva, Inverse Prob. **24**, 035020 (2008)
37. R. Chartrand, W. Yin, in *Proceedings of the 2008 IEEE International Conference on Acoustics, Speech and Signal Processing (ICASSP)* (Las Vegas, Nevada, USA, March 30–April 4, 2008), pp. 3869–3872
38. E.J. Candes, M.B. Wakin, S.P. Boyd, J. Fourier Anal. Appl. **14**, 877–905 (2008)
39. Y. She, Electron. J. Stat. **3**, 384–415 (2009)
40. D. Krishnan, R. Fergus, in *Proceedings of the 23rd Annual Conference on Neural Information Processing Systems 2009* (Vancouver, British Columbia, Canada, 7–10 December 2009), pp. 1033–1041

41. W. Zuo, D. Meng, L. Zhang, X. Feng, D. Zhang, in *Proceedings of the 2013 IEEE International Conference on Computer Vision (ICCV)* (Sydney, NSW, Australia, 1–8 December 2013), pp. 217–224
42. O. Inam, M. Qureshi, S.A. Malik, H. Omer, Appl. Magn. Reson. **48**, 1055–1074 (2017)
43. N. Seiberlich, F. Breuer, M. Blaimer, P. Jakob, M. Griswold, Magn. Reson. Med. **59**, 930–935 (2008)
44. J. Petr, J. Kybic, in *Proceedings of Medical Imaging 2007: Image Processing* (San Diego, California, USA, 18–20 February 2007), vol. 6512, p. 651241
45. S.E. Ghrare, S.M. Shreef, Int Sch Sci Res Innov **6**, 641–643 (2012)
46. M. Uecker, F. Ong, J.I. Tamir, D. Bahri, P. Virtue, J.Y. Cheng, T. Zhang, M. Lustig, in *Proceedings of the 23rd Annual Meeting of the International Society for Magnetic Resonance in Medicine (ISMRM)* (Toronto, Ontario, Canada, 30 May–05 June 2015), vol. 23, p. 2486
47. M.F. Siddiqui, A.W. Reza, A. Shafique, H. Omer, J. Kanesan, Magn. Reson. Imaging **44**, 82–91 (2017)